*J. Fluid Mech.* (2026), *vol.* 1030, R4, doi:10.1017/jfm.2026.11293



# Multiple states in centrifugal convection

**Zhongzhi Yao**[1], **Mohammad Shah Emran**[1], **Andrei Teimurazov**[1], **Marvin Kriening**[1], **Jiaxing Song**[1] **and Olga Shishkina**[1]

[1]Max Planck Institute for Dynamics and Self-Organization, Am Fassberg 17, 37077 Göttingen, Germany

**Corresponding authors:** Zhongzhi Yao, zhongzhi.yao@ds.mpg.de; Olga Shishkina, olga.shishkina@ds.mpg.de

(Received 25 December 2025; revised 22 January 2026; accepted 22 January 2026)

We systematically investigate the multiplicity of flow states in centrifugal convection in water at about 40 °C with Prandtl number $Pr = 4.3$ in a vertically aligned annulus in which the inner radius, the gap between the cylinders and the height all coincide (6 cm). This leaves two independent control parameters: the thermal driving, quantified by the Rayleigh number $Ra$, and the rotation strength, expressed by the Froude number $Fr$. We explore the range $2 \times 10^5 \leq Ra \leq 10^7$ for $Fr = 10$ and 100 with direct numerical simulations (DNS). The states are characterised by the number of convection rolls in the mid-height cross-section. We show that the final state sensitively depends on the initial condition, leading to pronounced multistability and substantial variations in heat and momentum transport, while the range of attainable states is strongly restricted. We derive a theoretical estimate of the admissible roll numbers based on the Poincaré–Friedrichs inequality and demonstrate quantitative agreement with the DNS. We further show that, for larger $Ra$, the range of possible states shrinks systematically due to an elliptical instability, providing a predictive framework for the selection and disappearance of coherent roll states in centrifugal convection.

**Key words:** rotating turbulence, turbulent convection, nonlinear instability

## 1. Introduction

Wall-bounded turbulent flows operated at identical control parameters often exhibit multiple, qualitatively distinct states, each with its own structure and transport characteristics, while the range of possible states and the pathways governing transitions among them remain largely unknown (Avila, Barkley & Hof 2023; Lohse & Shishkina 2024). A fundamental manifestation of this behaviour is multistability, where, for a given set of control parameters, two or more distinct states are dynamically stable, and the

© The Author(s), 2026. Published by Cambridge University Press. This is an Open Access article, distributed under the terms of the Creative Commons Attribution licence (https://creativecommons.org/licenses/by/4.0/), which permits unrestricted re-use, distribution and reproduction, provided the original article is properly cited.



https://doi.org/10.1017/jfm.2026.11293 Published online by Cambridge University Press

system can remain in any one of them for an extended period (or even indefinitely). Such multistability is associated with pronounced flow-memory effects, and transitions between stable states typically require finite-amplitude perturbations to push the system from the basin of attraction of one state into that of another. Multiple statistically stationary states have been identified in different wall-bounded flows. Plane Couette flow, channel flow and pipe flow at transitional Reynolds numbers can all exhibit coexistence of laminar flow and localised turbulence at the same control parameters (Hof *et al.* 2006; Avila *et al.* 2011; Barkley 2016; Manneville 2016; Avila *et al.* 2023). Beyond this laminar–turbulent coexistence, distinct turbulent states with different large-scale organisation and transport properties have been documented, for example in Taylor–Couette flow (van Gils *et al.* 2011*a*,*b*; Huisman *et al.* 2014; van der Veen *et al.* 2016; Ostilla-Mónico *et al.* 2016), von Kármán swirling flows (Ravelet *et al.* 2004, 2008; Cortet *et al.* 2010; Faranda *et al.* 2017), rotating spherical Couette flow (Zimmerman, Triana & Lathrop 2011) and Couette flow with spanwise rotation (Xia *et al.* 2018).

Similar phenomena have been observed in thermally driven and geophysical flows. In thermal convection, multiple long-lived states can coexist and compete, leading to pronounced multistability in both laboratory and numerical settings (Xi & Xia 2008; van der Poel *et al.* 2011, 2012; Wang *et al.* 2018; Xie, Ding & Xia 2018; Favier, Guervilly & Knobloch 2019; Wang *et al.* 2020; Roche 2020; Zwirner, Tilgner & Shishkina 2020; Shishkina 2021; Couston, Nandaha & Favier 2022; Lohse & Shishkina 2023, 2024). Beyond laboratory-scale systems, multistability is likewise a robust feature of geophysical and astrophysical flows, including multiple equilibria of the thermohaline circulation (Broecker, Peteet & Rind 1985; Schmeits & Dijkstra 2001; Ganopolski & Rahmstorf 2002), alternative dynamo regimes in Earth's liquid metal core (Glatzmaiers & Roberts 1995; Li, Sato & Kageyama 2002; Olson *et al.* 2010; Sheyko, Finlay & Jackson 2016) and coexisting large-scale atmospheric flow patterns (Weeks *et al.* 1997; Bouchet & Simonnet 2009; Bouchet & Venaille 2012; Bouchet, Rolland & Simonnet 2019). Taken together, these examples demonstrate that multistability and multiple turbulent states are generic phenomena, spanning canonical shear-driven configurations, thermally driven convection and geophysical flows, and they motivate a systematic study of how many distinct convective states are admissible and how they are selected in a given thermal convection system.

In this paper we study multiple states in centrifugal convection (CC). The flow is realised in a vertically aligned cylindrical annulus, as conceptually proposed and successfully implemented in the experiments of Sun and co-workers (Jiang *et al.* 2020, 2022; Lai, Zhong & Sun 2025; Ren *et al.* 2025) and investigated in our direct numerical simulations (DNS) (Yao *et al.* 2025), with top and bottom solid walls, a cooled inner cylindrical sidewall and a heated outer cylindrical sidewall, all subject to constant rotation about the vertical axis of the annulus (see figure 1). The CC is driven primarily by centrifugal buoyancy, with an additional contribution from gravitational buoyancy. Here we focus on multiple states in quasi-two-dimensional CC in laminar and weakly turbulent regimes, and demonstrate the coexistence of multiple statistically stable states in the parameter range $2 \times 10^5 \leq Ra \leq 10^7$ at Froude numbers $Fr = 10$ and 100. Each state is characterised by the number of convection rolls, which are azimuthally aligned and long-lived. We derive analytical estimates for the upper and lower bounds of the admissible roll numbers and show that they agree well with our DNS results.

## 2. Set-up, control and response parameters

Our CC set-up is a vertically aligned cylindrical annulus with top and bottom solid walls, a cooled inner sidewall and a heated outer sidewall, all rotating clockwise about the vertical



https://doi.org/10.1017/jfm.2026.11293 Published online by Cambridge University Press

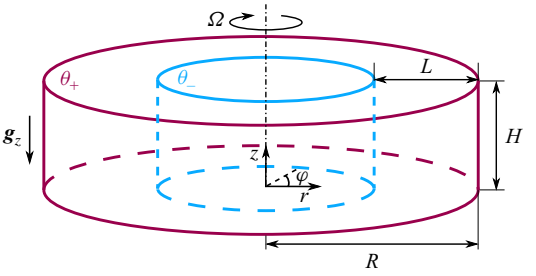



Figure 1. The CC set-up: a fluid-filled vertical annulus of height $H$, outer radius $R$ and gap width $L$ between inner (blue) and outer (pink) cylindrical walls, rotating clockwise at angular velocity $\Omega$ about its vertical axis; the inner and outer walls are kept at $\theta_-$ (blue) and $\theta_+$ (pink), with $\theta_+ > \theta_-$, the horizontal walls are adiabatic, no-slip conditions $\boldsymbol{u} = 0$ hold on all solid boundaries and gravity $\boldsymbol{g}_z$ points downward.

axis at constant angular velocity $\Omega \geq 0$ (see figure 1). The container has height $H$, outer radius $R$ and gap $L$ between the inner and outer vertical walls. The outer wall is at temperature $\theta_+$ and the inner wall at $\theta_-$, so that $\Delta \equiv \theta_+ - \theta_- > 0$. The horizontal walls are perfectly insulated (adiabatic), and the velocity satisfies no-slip boundary conditions $\boldsymbol{u} = 0$ on all walls. The two aspect ratios are $\Gamma_\phi \equiv 2\pi R/L = 4\pi$ and $\Gamma_H \equiv H/L = 1$. The fluid has fixed thermal expansion coefficient $\alpha$, kinematic viscosity $\nu$ and thermal diffusivity $\kappa$. The total acceleration is $\hat{g} \equiv (g_z^2 + g_\Omega^2)^{1/2}$, where $g_\Omega \equiv \Omega^2 R$ and $g_z$ is gravitational acceleration. The non-dimensional control parameters are the Rayleigh number $Ra$, Froude number $Fr$ and Prandtl number $Pr$:

$$Ra \equiv \alpha \hat{g} L^3 \Delta/(\kappa\nu), \quad Fr \equiv g_\Omega/g_z, \quad Pr \equiv \nu/\kappa = 4.3 \text{ (water at about 40 °C)}. \tag{2.1}$$

For fixed $\Gamma_\phi$ and $\Gamma_H$, the CC system has four independent control parameters: $Ra$, $Pr$, $Fr$ and either the Rossby number $Ro$ or the Ekman number $Ek$. However, for given fluid (so that all fluid properties and $Pr$ are fixed) and container geometry (including the aspect ratios $\Gamma_\phi$ and $\Gamma_H$, and the physical outer radius of the annulus $R$, so that the quantity $A \equiv 8\pi^2 \Gamma_\phi^{-2} (g_z R^3/(\nu\kappa))^{1/2}$ is also fixed), the CC system has only two independent parameters: one for the thermal driving, $Ra$, and one for the rotation strength, here chosen as $Fr$. The other rotation parameters become dependent parameters, as $Ro \equiv \sqrt{\alpha \hat{g} L \Delta}/(2\Omega L) = A^{-1}\sqrt{Ra/Fr}$ and $Ek \equiv \nu/(2\Omega L^2) = A^{-1}\sqrt{Pr/Fr}$.

The main response parameters in the system are the Nusselt and Reynolds numbers:

$$Nu = r\kappa^{-1}\Delta^{-1} \log(1 - 2\pi/\Gamma_\phi)\big[\langle u_r\theta\rangle_{\varphi,z,t} - \kappa\,\partial_r\langle\theta\rangle_{\varphi,z,t}\big], \quad Re = L\,\nu^{-1}\langle \boldsymbol{u}\cdot\boldsymbol{u}\rangle^{1/2}, \tag{2.2}$$

where $\boldsymbol{u}$ is the velocity field, $\theta$ the temperature, reduced by the arithmetic mean of the smallest ($\theta_-$) and largest ($\theta_+$) boundary temperatures, and $\langle\cdot\rangle$ the time and volume average.

## 3. Governing equations and DNS

The dimensionless Oberbeck–Boussinesq equations are obtained using the outer radius $R$ as length scale, the free-fall velocity $u_{ff} \equiv (\alpha \hat{g} R \Delta)^{1/2}$ as velocity scale, the free-fall time $R/u_{ff}$ as time scale, the temperature difference $\Delta$ as temperature scale, and $\rho\alpha\hat{g}R\Delta$ as pressure scale. The non-dimensional governing equations then read as follows: $\boldsymbol{\nabla}\cdot\boldsymbol{u} = 0$,



https://doi.org/10.1017/jfm.2026.11293 Published online by Cambridge University Press

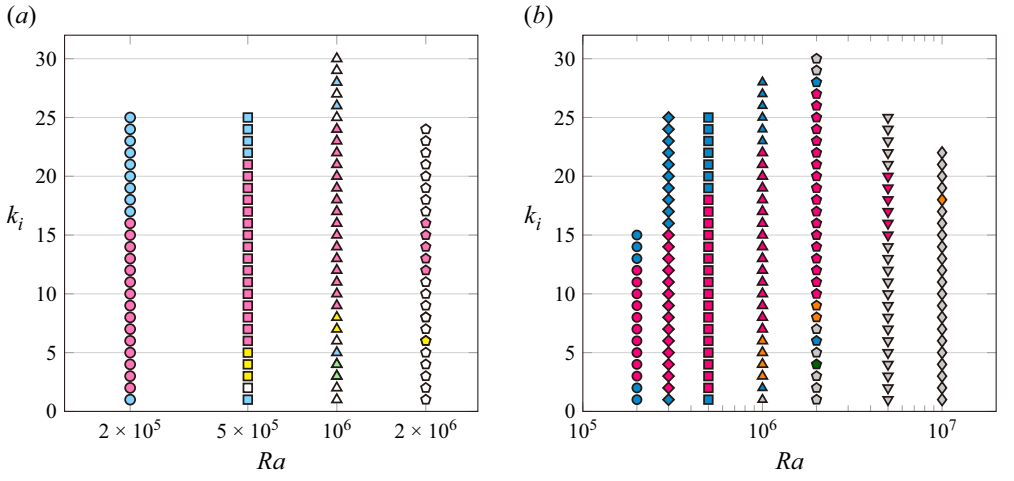



Figure 2. Phase diagram of the conducted DNS in the $(Ra, k_i)$ parameter space for (*a*) $Fr = 10$ and (*b*) $Fr = 100$. Different symbol shapes indicate different $Ra$, and colours denote the final flow state after 3000 time units: pink – flow with a persistent coherent roll structure, where initial ($k_i$) and final ($k$) roll numbers coincide, $k = k_i$, and $\sigma_{Nu} \le 0.1$, $\sigma_{Re} \le 0.1$, with $\sigma_{Nu}^2 \equiv \langle (Nu_t - Nu)^2 \rangle_t$ and $\sigma_{Re}^2 \equiv \langle (Re_t - Re)^2 \rangle_t$, where $Nu_t$ and $Re_t$ are the instantaneous Nusselt and Reynolds numbers and $\langle \cdot \rangle_t$ represents time averaging; orange – flow with $k = k_i$, but $\sigma_{Nu} > 0.1$ or $\sigma_{Re} > 0.1$; blue – flow with $k \neq k_i$ and $\sigma_{Nu} \le 0.1$, $\sigma_{Re} \le 0.1$; white and grey – chaotic flow; green – flow initialised with (3.2) is chaotic, but is steady with $k = k_i$ if initialised from a flow at a different $Ra$ (see the end of the supplementary material available at https://doi.org/10.1017/jfm.2026.11293). The same symbol and colour coding is used in all figures of the paper.

$$D_t \boldsymbol{u} = -\boldsymbol{\nabla} p + \sqrt{\frac{8\pi^3}{\Gamma_\phi^3}\frac{Pr}{Ra}}\nabla^2 \boldsymbol{u} + \frac{1}{\sqrt{1+Fr^2}}\theta \boldsymbol{e}_z - \sqrt{\frac{\Gamma_\phi}{2\pi}} Ro^{-1} \boldsymbol{u} \times \boldsymbol{e}_z - \frac{Fr}{\sqrt{1+Fr^2}}\theta r \boldsymbol{e}_r,$$
$$D_t \theta = \sqrt{8\pi^3/(\Gamma_\phi^3\, Pr\, Ra)}\, \nabla^2 \theta, \qquad D_t \equiv \partial_t + (\boldsymbol{u} \cdot \boldsymbol{\nabla}), \tag{3.1}$$

where $p$ is the pressure and $\boldsymbol{e}_z$ and $\boldsymbol{e}_r$ are the unit vectors in the vertical and radial directions, respectively. The boundary conditions are no-slip for the velocity at all walls, adiabatic at the top and bottom surfaces and isothermal at the vertical sidewalls ($\theta_-$ and $\theta_+$).

To conduct DNS of CC, we use the latest version of the finite-volume code goldfish, which is fourth-order in space and third-order Runge–Kutta in time (Shishkina *et al.* 2015; Reiter *et al.* 2021, 2022). The code handles annular geometries (Yao *et al.* 2025), internal boundaries (Wagner & Shishkina 2015; Emran & Shishkina 2020), specific boundary conditions (Ecke, Zhang & Shishkina 2022; Zhang *et al.* 2024) and rotation with careful treatment of centrifugal effects (Zhang *et al.* 2020, 2021).

The computational non-equidistant staggered grids with $N_r \times N_\phi \times N_z = 128 \times 512 \times 128$ for $Ra \le 2 \times 10^6$ and $192 \times 768 \times 192$ for $2 \times 10^6 < Ra \le 10^7$ are sufficiently fine to resolve both the Kolmogorov and (for large $Pr$ more restrictive) Batchelor microscales. Within each thermal or viscous boundary layer, at least 10 grid points are used to satisfy DNS resolution criteria (Shishkina *et al.* 2010). An additional grid refinement study for selected cases, with the grid resolution increased by a factor of at least 2.5, leads to changes in the Nusselt number $Nu$ of less than 1 % over long-time averages.

To investigate multiple states in CC dominated by centrifugal buoyancy, we consider $Fr = 10$ and 100 and the range $2 \times 10^5 \le Ra \le 10^7$. In all our DNS, we fix $Pr = 4.3$ and the quantity $A$ by setting the outer annulus radius to $R = 6$ cm. For each set of control parameters, between 15 and 30 different initial conditions are tested (see figure 2).



https://doi.org/10.1017/jfm.2026.11293 Published online by Cambridge University Press

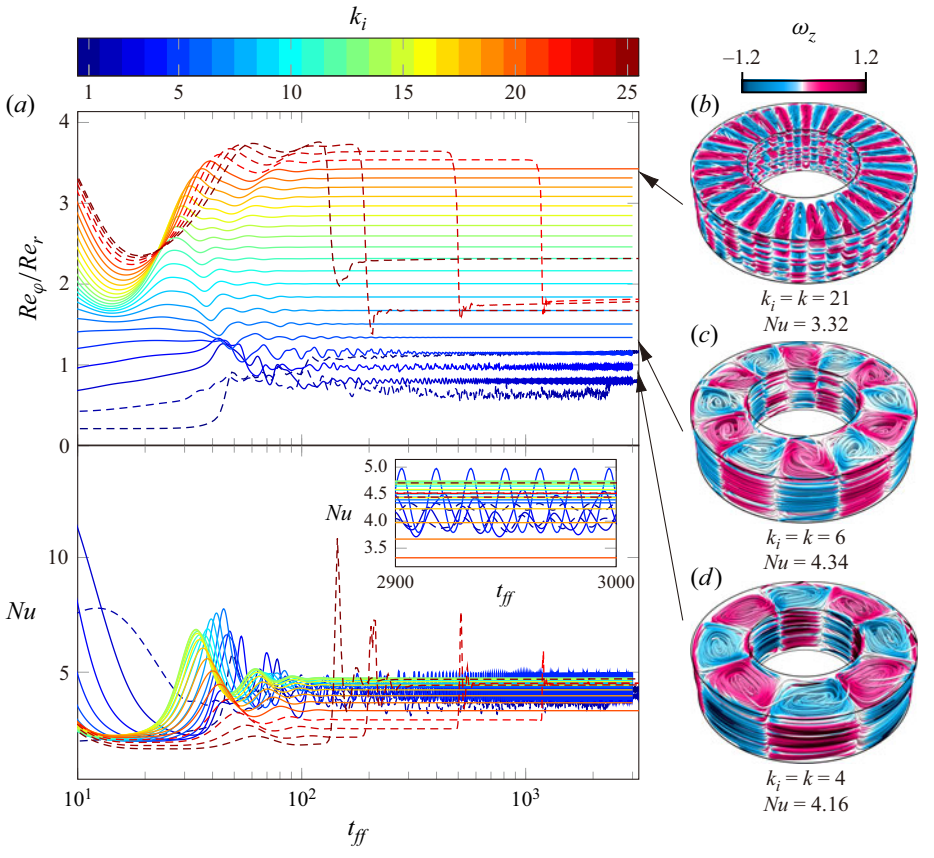



Figure 3. (*a*) Time evolution of $Re_\varphi/Re_r$ and $Nu$ for different initial roll-pair numbers $k_i$ at $Ra = 5 \times 10^5$ and $Fr = 10$. Among different numbers of initial rolls $k_i$, the persistent cases ($k = k_i$, shown with solid lines) are only for $3 \le k_i \le 21$. Non-persistent cases ($k \neq k_i$) are shown with dashed lines. (*b–d*) Instantaneous flow fields visualised with trajectories of passive tracer particles, coloured by the $z$ component of the vorticity, $\omega_z$, for three representative cases.

We initialise each flow with a zero velocity field, while the initial temperature field $\theta(t = 0, r, \varphi, z) = \theta_i(r, \varphi)$ mimics different numbers $k_i$ of roll pairs in the azimuthal direction:

$$\theta_i(r, \varphi) = \pi^{-1} \sin(k_i \varphi) \sin(2\pi r) + 2r - 3/2. \tag{3.2}$$

This function satisfies the boundary conditions $\theta_i|_{r=1/2} = -1/2$ and $\theta_i|_{r=1} = 1/2$, and is monotonic in the radial direction ($\partial\theta_i/\partial r \ge 0$). The mid-height cross-sections of the initial flows and of the flows after 3000 time units are provided in the supplementary material available at https://doi.org/10.1017/jfm.2026.11293.

## 4. The DNS results

Figure 2 summarises the initial and final states of all studied cases. Some flows retain the initial number of rolls (pink and orange), some become statistically steady but with a different final number of roll pairs $k$ than the initial $k_i$ (blue), some become chaotic (grey and white) and a subset of these chaotic cases can be brought to a statistically steady flow with a persistent roll structure when initialised from a steady flow at a different $Ra$ with $k_i$ roll pairs (green). An example of the temporal flow development is shown in figure 3 for



https://doi.org/10.1017/jfm.2026.11293 Published online by Cambridge University Press

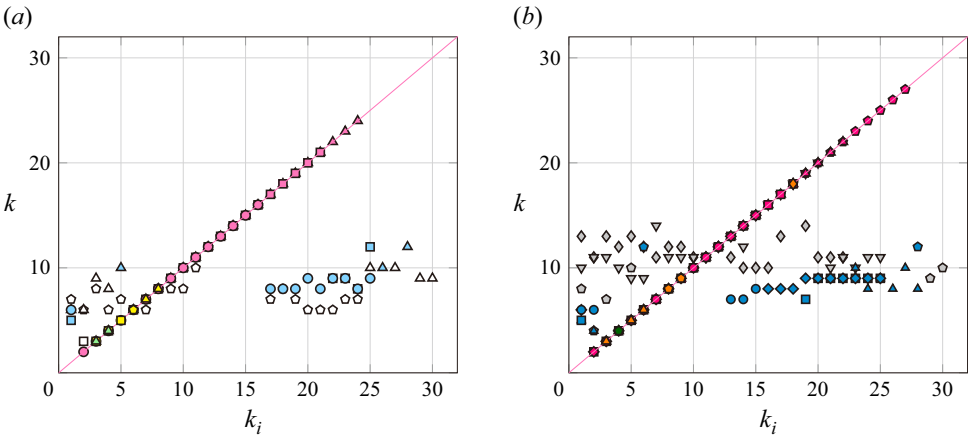



Figure 4. Final number of roll pairs $k$ for different initial numbers of roll pairs $k_i$ at $Fr = 10$ (*a*) and $Fr = 100$ (*b*). Symbol meanings are the same as in figure 2.

$Ra = 5 \times 10^5$ and $Fr = 10$. Changes in the roll number from its initial value are reflected in abrupt variations of $Nu$ and of the ratio between the Reynolds numbers based on the azimuthal and radial velocity components, $Re_\varphi/Re_r$. Such changes can occur even after $10^3$ free-fall time units, indicating that the time required for a persistent coherent roll structure to develop does not scale with the convective time but rather with the diffusive time.

The final number of roll pairs $k$ obtained from different initial roll counts $k_i$ is shown in figure 4. Persistent cases lie along the diagonal, whereas non-persistent cases are scattered between $k = 6$ and 14. Although the resulting $k$ values for non-persistent cases may appear random, they can be understood by examining the associated heat and momentum transport.

The results for the heat and momentum transport, expressed by $Nu$ and $Re$ as functions of the initial number of roll pairs $k_i$, are shown in figure 5 and can be summarised as follows. For fixed $Fr$, persistent statistically steady flows (coloured symbols) occur only for small and moderate $Ra$, since at larger $Ra$ the flows become chaotic (white and grey symbols). For moderate $Ra$, both $Nu$ and $Re$ increase with growing $k_i$ (i.e. decreasing aspect ratio of rolls, $\Gamma_r$), in agreement with previous findings for Rayleigh–Bénard convection (Wang *et al.* 2020); see the pink pentagons in figure 5(*a*,*c*) for $Ra = 2 \times 10^6$, $Fr = 10$, and down-pointing triangles in figure 5(*b*,*d*) for $Ra = 5 \times 10^6$, $Fr = 100$. With a further increase of $k_i$, the flow becomes chaotic and both $Nu$ and $Re$ drop to lower values (grey symbols). For small $Ra$, both $Nu$ and $Re$ likewise first increase with $k_i$, reach a maximum and then start to decrease owing to full laminarisation of the flow (see the remaining pink symbols in figure 5). In this case, very narrow rolls (very large $k$) are damped by viscosity, dissipation rises, the heat transport becomes more diffusive and the flow approaches a steady (or weakly unsteady) laminar state. For sufficiently large $k_i$, the flow can no longer sustain this high roll number and undergoes an abrupt structural change to a steady flow with a smaller number of rolls $k < k_i$ (blue symbols). During this transition, $Nu$ and $Re$ jump to values close to their maxima and thereafter remain almost independent of further increases in $k_i$.

The ranges of possible $Nu$ and $Re$ variations with $k_i$, as obtained in our DNS, are listed in table 1. The largest variations in $Nu$ and $Re$ for different $k_i$ occur at smaller $Ra$ (up to $\approx$67 % in $Nu$ for $Ra = 2 \times 10^5$). At our largest $Ra = 10^7$, they are much smaller (<4 % in $Nu$) but remain finite. Changes in $Nu$ are always larger than those in $Re$.



https://doi.org/10.1017/jfm.2026.11293 Published online by Cambridge University Press

| $Ra$ | $Fr$ | $Nu_{max}$ | $Nu_{min}$ | $(Nu_{max}-Nu_{min})/Nu_{max}$ (%) | $Re_{max}$ | $Re_{min}$ | $(Re_{max}-Re_{min})/Re_{max}$ (%) |
|---|---|---|---|---|---|---|---|
| $2\times10^5$ | 10 | 3.35 | 2.01 | 66.8 | 5.76 | 3.65 | 57.9 |
| $5\times10^5$ | 10 | 4.74 | 3.32 | 42.7 | 11.05 | 8.14 | 35.8 |
| $10^6$ | 10 | 5.99 | 4.85 | 23.4 | 16.30 | 13.37 | 22.2 |
| $2\times10^6$ | 10 | 7.24 | 6.22 | 16.5 | 26.24 | 24.25 | 8.2 |
| $2\times10^5$ | 100 | 2.81 | 1.93 | 45.4 | 3.81 | 2.74 | 39.0 |
| $3\times10^5$ | 100 | 3.31 | 2.09 | 58.4 | 5.27 | 3.59 | 46.6 |
| $5\times10^5$ | 100 | 3.94 | 2.47 | 59.8 | 7.22 | 5.02 | 43.8 |
| $10^6$ | 100 | 5.44 | 4.32 | 26.1 | 12.90 | 10.75 | 20.4 |
| $2\times10^6$ | 100 | 6.96 | 5.68 | 22.5 | 19.88 | 16.38 | 21.4 |
| $5\times10^6$ | 100 | 9.26 | 7.98 | 16.1 | 36.01 | 34.38 | 4.8 |
| $10^7$ | 100 | 10.51 | 10.12 | 3.9 | 54.40 | 54.18 | 0.5 |

Table 1. Comparison of the maximum ($Nu_{max}$, $Re_{max}$) and minimum ($Nu_{min}$, $Re_{min}$) values of the Nusselt and Reynolds numbers for all cases at the same control parameters but different initial conditions.

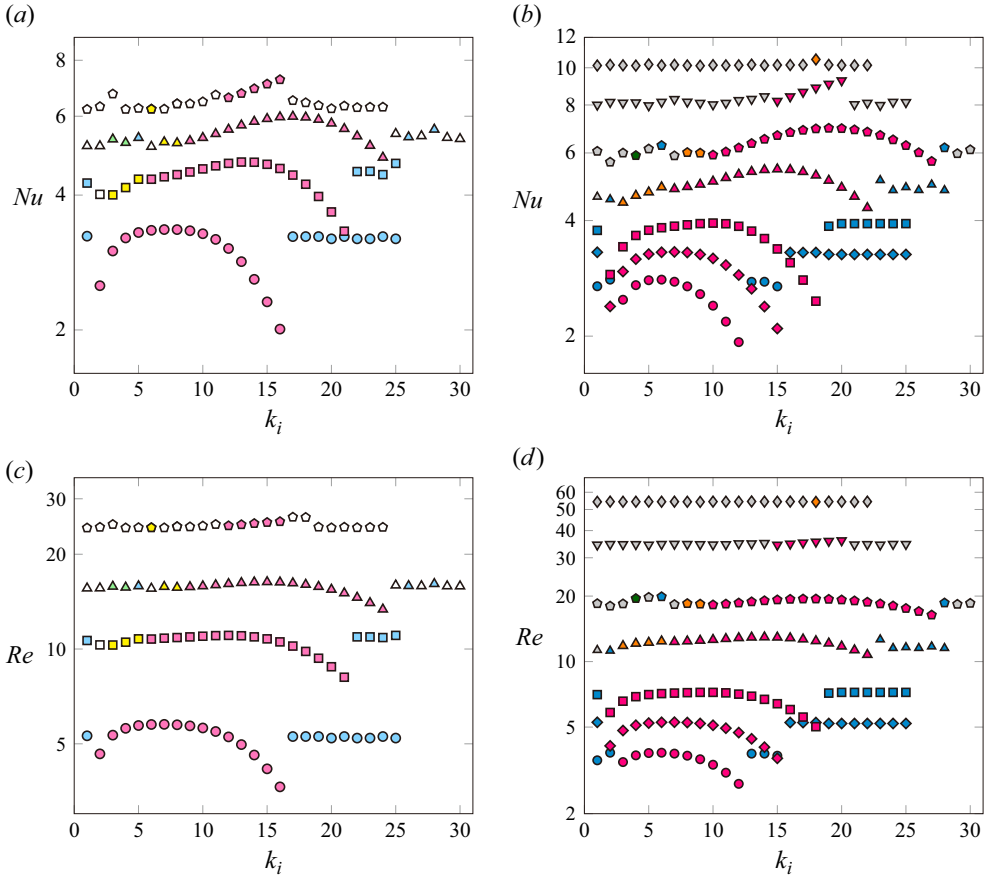



Figure 5. Nusselt numbers ($a$, $b$) and Reynolds numbers ($c$, $d$) for different initial numbers of roll pairs $k_i$ at $Fr = 10$ ($a$, $c$) and $Fr = 100$ ($b$, $d$). Symbol meanings are the same as in figure 2.

https://doi.org/10.1017/jfm.2026.11293 Published online by Cambridge University Press

## 5. Estimation of the feasible number of azimuthal rolls

In figure 6(*a*,*b*) we show the number of roll pairs $k$ in CC flows with coherent roll structures as functions of $Ra$. Flows in which the initial and final roll numbers coincide ($k = k_i$) are marked in pink and orange, while those with $k \neq k_i$ are marked in blue. Green symbols denote flows that are chaotic when initialised with (3.2) and are steady when initialised with a flow with $k$ roll pairs at a different $Ra$. For fixed $Fr$, the range of possible states is broad at small $Ra$ and shrinks as $Ra$ increases. How can we estimate these ranges?

### 5.1. *Estimate of the maximal number of roll pairs from Poincaré–Friedrichs inequality*

According to the Poincaré–Friedrichs inequality, for a dimensionless velocity $\boldsymbol{u}$ that vanishes on the boundary, one has $\hat{\lambda}_{min}\langle \boldsymbol{u}^2\rangle \leq \langle(\boldsymbol{\nabla u})^2\rangle$, where $\hat{\lambda}_{min}$ is the smallest positive eigenvalue of the Laplacian, associated with an eigenfunction $f$ that has a non-zero projection on at least one component of the velocity $u$ (i.e. $\langle uf\rangle \neq 0$), and $\lambda_{min} = L^2\hat{\lambda}_{min}$ its dimensionless analogue. Introducing the integral quantity

$$B \equiv Re^2 / \left(L^4 \nu^{-3} \epsilon_u\right), \tag{5.1}$$

where $\epsilon_u \equiv \nu\langle(\boldsymbol{\nabla u})^2\rangle$ is the averaged kinetic energy dissipation rate, we obtain $\lambda_{min} B \leq 1$.

Now, to estimate how many azimuthal rolls can fit inside the annulus, we consider the Laplace eigenvalue problem with zero boundary conditions on the solid walls, and $2\pi$-periodicity in the $\varphi$ direction. We seek eigenfunctions of $(-\nabla^2)$ that exhibit a prescribed number of oscillations in the azimuthal direction. Specifically, we consider the eigenvalue problem $-\nabla^2 f = \lambda f$ in $\Omega$, subject to the appropriate boundary conditions. The Laplacian is then expressed in cylindrical coordinates, $\nabla^2 f = r^{-1}\partial_r(r\,\partial_r f) + r^{-2}\partial_\varphi^2 f + \partial_z^2 f$. The eigenfunctions separate in $(r, \varphi, z)$, $f = P(r)\,\Phi(\varphi)\,Z(z)$, so that the vertical problem with zero conditions at $z = 0$, $H/L$ gives $Z_n(z) = \sin(n\pi z L/H)$, $n \geq 1$, and the azimuthal problem with $2\pi$-periodicity yields $\Phi_k(\varphi) = \cos(k\varphi)$ or $\sin(k\varphi)$. Such a function undergoes exactly $2k$ sign changes when $\varphi$ runs from 0 to $2\pi$; hence $k$ corresponds directly to the number of roll pairs. Introducing $\varkappa^2 \equiv \lambda - (n\pi L/H)^2$, we obtain the radial equation $r^2 P'' + r P' + (\varkappa^2 r^2 - k^2)\,P = 0$, whose solutions are $P(r) = a J_k(\varkappa r) + b Y_k(\varkappa r)$, with $J_k$ and $Y_k$ being the Bessel functions of the first and second kind. The Dirichlet boundary conditions at $r = R/L - 1$ and $r = R/L$ impose $a J_k(\varkappa(R/L-1)) + b Y_k(\varkappa(R/L-1)) = 0$ and $a J_k(\varkappa R/L) + b Y_k(\varkappa R/L) = 0$, for which non-trivial solutions for $a$ and $b$ exist only if

$$F_k(\varkappa) \equiv J_k(\varkappa(R/L-1))\,Y_k(\varkappa R/L) - J_k(\varkappa R/L)\,Y_k(\varkappa(R/L-1)) = 0. \tag{5.2}$$

For each triple $(k, j, n)$, the eigenvalue equals $\lambda_{k,j,n} = \varkappa_{k,j}^2 + (n\pi L/H)^2$, where $\varkappa_{k,j}$ is the $j$th positive root of $F_k(\varkappa) = 0$. The smallest eigenvalue for a given $k$ is obtained for $j = n = 1$. For the annulus considered in our DNS, the radial condition (5.2) simplifies to

$$F_k(\varkappa) = J_k(\varkappa)\,Y_k(2\varkappa) - J_k(2\varkappa)\,Y_k(\varkappa) = 0. \tag{5.3}$$

The lowest eigenvalue for the wavenumber $k$ and the corresponding eigenfunction are

$$\lambda_{min}(k) = \varkappa_{k,1}^2 + \pi^2, \quad \text{where } \varkappa_{k,1} \text{ is the first positive root of (5.3)}, \tag{5.4}$$

and $f_k = [J_k(\varkappa_{k,1} r) Y_k(2\varkappa_{k,1}) - Y_k(\varkappa_{k,1} r) J_k(2\varkappa_{k,1})]\sin(k\varphi)\sin(\pi z)$, respectively.

By solving the inverse problem numerically, one can determine which values of $k$ are admissible for a prescribed value of $B$. More precisely, for each $k$ the eigenvalue $\lambda_{min}(k)$ is obtained from (5.4), which directly yields the maximal value of $B$, $B_{max} = \lambda_{min}^{-1}(k)$, for which a flow state with $2k$ azimuthal rolls can exist. From this, one can readily



https://doi.org/10.1017/jfm.2026.11293 Published online by Cambridge University Press

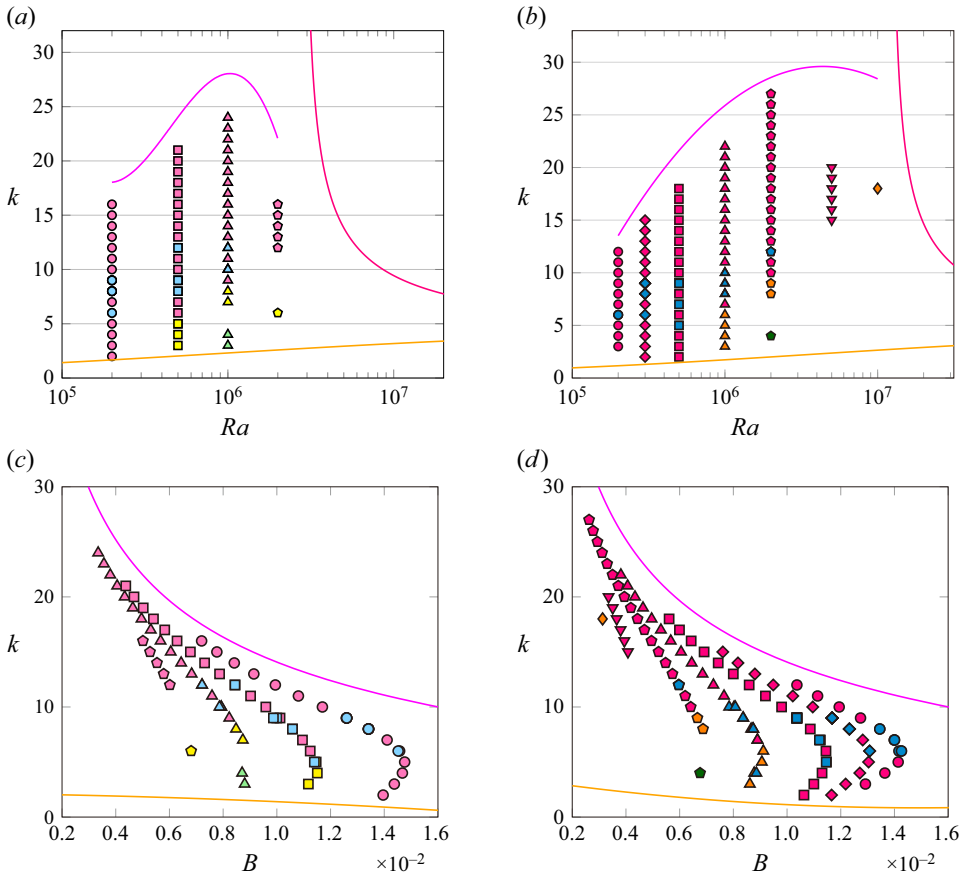



Figure 6. Number of roll pairs $k$ in CC flows with coherent roll structures after 3000 time units, as functions of $Ra$ ($a$, $b$) and $B$ ($c$, $d$) for $Fr = 10$ ($a$, $c$) and $Fr = 100$ ($b$, $d$). Symbols, DNS results; lines, theoretical upper bounds from the Poincaré–Friedrichs inequality (magenta) and upper and lower bounds (5.7) from the elliptical stability criteria (red and yellow). Symbol meanings are the same as in figure 2, with most blue symbols overlapping the pink ones; chaotic cases are not shown.

evaluate the maximal number of roll pairs $k_{max}$ that can develop for a given $B$. In figure 6($c$,$d$) this theoretical estimate is shown by the magenta lines and exhibits very good agreement with the DNS data. The dependence of $k_{max}$ on $B$ can be directly translated into a dependence on $Ra$. Since $k_{max}(B)$ is a monotonically decreasing function, for each $Ra$ we take the smallest value of $B$ obtained in the DNS at that $Ra$ and thus obtain the corresponding dependence $k_{max}(Ra)$ for each $Fr$. These dependences are plotted in figure 6($a$,$b$) as magenta lines; they show good agreement with the DNS data and provide reliable estimates of the maximal possible number of roll pairs $k$ in statistically steady flows with coherent roll structures, using only the minimal value of the integral quantity $B$ for given $Ra$ and $Fr$.

### 5.2. *Bounds on the number of roll pairs from elliptical instability*

The three-dimensional destabilisation of vortices with stretched elliptical streamlines of the aspect ratio $\Gamma_r > 1$ is usually attributed to the elliptical instability (Bayly 1986; Waleffe 1990; Zwirner *et al.* 2020). For a columnar vortex with angular velocity $\omega$ and ellipticity $\beta \equiv (\Gamma_r^2 - 1)/(\Gamma_r^2 + 1)$, inviscid asymptotics give a maximum growth rate $\sigma$ of order $\beta\omega$,



https://doi.org/10.1017/jfm.2026.11293 Published online by Cambridge University Press

while viscosity introduces a damping of order $E^{1/2}\omega$ with the vortex Ekman number

$$E \equiv \nu/\left(\omega D^2\right) \approx (L/D)^2\sqrt{B}/Re, \quad D^2 \equiv L^2\left(\Gamma_r^2+1\right)/2, \tag{5.5}$$

leading to $\sigma \approx (c_1\,\beta - c_2\,E^{1/2})\omega$ with $c_1 > 0$ and $c_2 > 0$ (Hollerbach & Kerswell 1995; Lacaze, Gal & Dizès 2005). Thus the stretched roll flow can sustain only if $\beta < (c_2/c_1)E^{1/2}$, i.e.

$$\left(\Gamma_r^2-1\right)^2 / \left(\Gamma_r^2+1\right) < 2\,(c_2/c_1)^2\,\sqrt{B}/Re \equiv s. \tag{5.6}$$

Estimating $\Gamma_r \approx 3\pi/(2k)$, from relation (5.6) we obtain the lower and upper bounds for $k$:

$$3\pi\left(4+2s+2\left(s^2+8s\right)^{1/2}\right)^{-1/2} \le k \le 3\pi\left(4+2s-2\left(s^2+8s\right)^{1/2}\right)^{-1/2}. \tag{5.7}$$

Our DNS data (albeit for only two values of $Fr$) suggest that $s \approx 10^5 Fr^{0.3} Ra^{-0.8}$, showing a clear decrease of $s$ with increasing $Ra$. Since the range (5.7) of admissible $k$ values around $k = 3\pi/2$ (corresponding to the roll aspect ratio $\Gamma_r = 1$) shrinks as $s$ decreases, we conclude that, for any fixed $Fr \gg 1$, the range of possible statistically steady states with coherent roll structures narrows with increasing $Ra$ (see figure 6, red and yellow lines).

## 6. Conclusions

We have systematically investigated the multiplicity of flow states in CC in a vertical annulus by means of DNS over the parameter range $2 \times 10^5 \le Ra \le 10^7$ and $Fr = 10,\ 100$ at $Pr = 4.3$ and fixed geometry. By varying the initial number of roll pairs $k_i$ in the azimuthal direction, we explored 278 cases and mapped out a detailed phase diagram in the $(Ra, k_i)$ plane. For a wide range of parameters, the system exhibits multiple statistically steady states with different numbers of coherent azimuthal roll pairs at the same control parameters, as well as chaotic states and cases in which the final roll number ($k$) differs from the initial one ($k_i$). In some parameter regimes, states with coherent roll structures can only be obtained when the flow is initialised from another statistically steady state at a different $Ra$, highlighting pronounced flow-memory and path-dependence effects.

The multiplicity of states is reflected in substantial variations in heat and momentum transport. At small and moderate $Ra$, the Nusselt and Reynolds numbers can differ by up to, respectively, ≈67 % and ≈58 % between different initial conditions for fixed $(Ra, Fr)$, with the largest values typically associated with intermediate numbers $k_i$. For too small or too large $k_i$, the flow either laminarises to a state with a different number of rolls, $k \neq k_i$, or becomes chaotic, and $Nu$ and $Re$ are reduced. As $Ra$ increases, the range of initial conditions that lead to persistent coherent roll states shrinks, and at sufficiently high $Ra$ only chaotic dynamics remains, so that the dependence of $Nu$ and $Re$ on $k_i$ becomes weak.

We have developed a theoretical framework that predicts which roll numbers are admissible for given control parameters. An upper bound on $k$ is derived from a global constraint based on the Poincaré–Friedrichs inequality. Complementary bounds on admissible $k$ follow from the criterion for elliptical instability of the vortical rolls; this instability eliminates states with too few or too many rolls and causes the range of roll states to shrink as $Ra$ increases. These theoretical predictions are consistent with the DNS results.

**Supplementary material.** Supplementary material is available at https://doi.org/10.1017/jfm.2026.11293.



https://doi.org/10.1017/jfm.2026.11293 Published online by Cambridge University Press

**Acknowledgements.** The authors gratefully acknowledge stimulating discussions with D. Lohse and C. Sun. The authors also acknowledge the computational resources provided by the Max Planck Computing and Data Facility.

**Funding.** This work was supported by the German Research Foundation under grants Sh405/20, Sh405/22, and So2399/2. Open access funding provided by Max Planck Society.

**Declaration of interests.** The authors report no conflict of interests.

## References

AVILA, K., MOXEY, D., DE LOZAR, A., AVILA, M., BARKLEY, D. & HOF, B. 2011 The onset of turbulence in pipe flow. *Science* **333** (6039), 192–196.

AVILA, M., BARKLEY, D. & HOF, B. 2023 Transition to turbulence in pipe flow. *Annu. Rev. Fluid Mech.* **55**, 575–602.

BARKLEY, D. 2016 Theoretical perspective on the route to turbulence in a pipe. *J. Fluid Mech.* **803**, P1.

BAYLY, B.J. 1986 Three-dimensional instability of elliptical flow. *Phys. Rev. Lett.* **57**, 2160–2163.

BOUCHET, F., ROLLAND, J. & SIMONNET, E. 2019 Rare event algorithm links transitions in turbulent flows with activated nucleations. *Phys. Rev. Lett.* **122** (7), 074502.

BOUCHET, F. & SIMONNET, E. 2009 Random changes of flow topology in two-dimensional and geophysical turbulence. *Phys. Rev. Lett.* **102** (9), 094504.

BOUCHET, F. & VENAILLE, A. 2012 Statistical mechanics of two-dimensional and geophysical flows. *Phys. Rep.* **515** (5), 227–295.

BROECKER, W.S., PETEET, D.M. & RIND, D. 1985 Does the ocean–atmosphere system have more than one stable mode of operation? *Nature* **315** (6014), 21.

CORTET, P., CHIFFAUDEL, A., DAVIAUD, F. & DUBRULLE, B. 2010 Experimental evidence of a phase transition in a closed turbulent flow. *Phys. Rev. Lett.* **105**, 214501.

COUSTON, L.-A., NANDAHA, J. & FAVIER, B. 2022 Competition between Rayleigh–Bénard and horizontal convection. *J. Fluid Mech.* **947**, A13.

ECKE, R.E., ZHANG, X. & SHISHKINA, O. 2022 Connecting wall modes and boundary zonal flows in rotating Rayleigh–Bénard convection. *Phys. Rev. Fluids* **7**, L011501.

EMRAN, M.S. & SHISHKINA, O. 2020 Natural convection in cylindrical containers with isothermal ring-shaped obstacles. *J. Fluid Mech.* **882**, A3.

FARANDA, D., SATO, Y., SAINT-MICHEL, B., WIERTEL, C., PADILLA, V., DUBRULLE, B. & DAVIAUD, F. 2017 Stochastic chaos in a turbulent swirling flow. *Phys. Rev. Lett.* **119** (1), 014502.

FAVIER, B., GUERVILLY, C. & KNOBLOCH, E. 2019 Subcritical turbulent condensate in rapidly rotating Rayleigh–Bénard convection. *J. Fluid Mech.* **864**, R1.

GANOPOLSKI, A. & RAHMSTORF, S. 2002 Abrupt glacial climate changes due to stochastic resonance. *Phys. Rev. Lett.* **88** (3), 038501.

VAN GILS, D.P.M., BRUGGERT, G.W., LATHROP, D.P., SUN, C. & LOHSE, D. 2011*a* The Twente turbulent Taylor–Couette ($T^3C$) facility: strongly turbulent (multi-phase) flow between independently rotating cylinders. *Rev. Sci. Instrum.* **82**, 025105.

VAN GILS, D.P.M., HUISMAN, S.G., BRUGGERT, G.-W., SUN, C. & LOHSE, D. 2011*b* Torque scaling in turbulent Taylor-Couette flow with co-and counterrotating cylinders. *Phys. Rev. Lett.* **106**, 024502.

GLATZMAIERS, G.A. & ROBERTS, P.H. 1995 A three-dimensional self-consistent computer simulation of a geomagnetic field reversal. *Nature* **377** (6546), 203–209.

HOF, B., WESTERWEEL, J., SCHNEIDER, T.M. & ECKHARDT, B. 2006 Finite lifetime of turbulence in shear flow. *Nature* **443**, 59–62.

HOLLERBACH, R. & KERSWELL, R.R. 1995 Oscillatory internal shear layers in rotating and precessing flows. *J. Fluid Mech.* **298**, 327–339.

HUISMAN, S.G., VAN DER VEEN, R.C.A., SUN, C. & LOHSE, D. 2014 Multiple states in highly turbulent Taylor–Couette flow. *Nat. Commun.* **5**, 3820.

JIANG, H., WANG, D., LIU, S. & SUN, C. 2022 Experimental evidence for the existence of the ultimate regime in rapidly rotating turbulent thermal convection. *Phys. Rev. Lett.* **129**, 204502.

JIANG, H., ZHU, X., WANG, D., HUISMAN, S.G. & SUN, C. 2020 Supergravitational turbulent thermal convection. *Sci. Adv.* **6** (40), eabb8676.

LACAZE, L., GAL, P.LE & DIZÈS, S.LE 2005 Elliptical instability of the flow in a rotating shell. *Phys. Earth Planet. Inter.* **151**, 194–205.

LAI, R., ZHONG, J. & SUN, C. 2025 Gravity drives the flow within the Stewartson layer in centrifugal convection. *J. Fluid Mech.* **1022**, A43.



https://doi.org/10.1017/jfm.2026.11293 Published online by Cambridge University Press

LI, J., SATO, T. & KAGEYAMA, A. 2002 Repeated and sudden reversals of the dipole field generated by a spherical dynamo action. *Science* **295** (5561), 1887–1890.
LOHSE, D. & SHISHKINA, O. 2023 Ultimate turbulent thermal convection. *Phys. Today* **76** (11), 26–32.
LOHSE, D. & SHISHKINA, O. 2024 Ultimate Rayleigh–Bénard turbulence. *Rev. Mod. Phys.* **96** (3), 035001.
MANNEVILLE, P. 2016 Transition to turbulence in wall-bounded flows: Where do we stand? *Mech. Engng Rev.* **3** (2), 15–00684–15–00684.
OLSON, P.L., COE, R.S., DRISCOLL, P.E., GLATZMAIER, G.A. & ROBERTS, P.H. 2010 Geodynamo reversal frequency and heterogeneous core–mantle boundary heat flow. *Phys. Earth Planet. Inter.* **180** (1–2), 66–79.
OSTILLA-MÓNICO, R., LOHSE, D. & VERZICCO, R. 2016 Effect of roll number on the statistics of turbulent Taylor–Couette flow. *Phys. Rev. Fluids* **1** (5), 054402.
VAN DER POEL, E.P., STEVENS, R.J.A.M. & LOHSE, D. 2011 Connecting flow structures and heat flux in turbulent Rayleigh–Bénard convection. *Phys. Rev. E* **84**, 045303(R).
VAN DER POEL, E.P., STEVENS, R.J.A.M., SUGIYAMA, K. & LOHSE, D. 2012 Flow states in two-dimensional Rayleigh–Bénard convection as a function of aspect ratio and Rayleigh number. *Phys. Fluids* **24**, 085104.
RAVELET, F., *et al.* 2008 Chaotic dynamos generated by a turbulent flow of liquid sodium. *Phys. Rev. Lett.* **101** (7), 074502.
RAVELET, F., MARIÉ, L., CHIFFAUDEL, A. & DAVIAUD, F. 2004 Multistability and memory effect in a highly turbulent flow: experimental evidence for a global bifurcation. *Phys. Rev. Lett.* **93**, 164501.
REITER, P., ZHANG, X. & SHISHKINA, O. 2022 Flow states and heat transport in Rayleigh–Bénard convection with different sidewall boundary conditions. *J. Fluid Mech.* **936**, A32.
REITER, P., ZHANG, X., STEPANOV, R. & SHISHKINA, O. 2021 Generation of zonal flows in convective systems by travelling thermal waves. *J. Fluid Mech.* **913**, A13.
REN, L., ZHONG, J., LAI, R. & SUN, C. 2025 Physical mechanism behind the early onset of the ultimate state in supergravitational centrifugal thermal convection. arXiv: 2509.14800.
ROCHE, P.-E. 2020 The ultimate state of convection: a unifying picture of very high Rayleigh numbers experiments. *New J. Phys.* **22** (7), 073056.
SCHMEITS, M.J. & DIJKSTRA, H.A. 2001 Bimodal behavior of the Kuroshio and the Gulf Stream. *J. Phys. Oceanogr.* **31** (12), 3435–3456.
SHEYKO, A., FINLAY, C.C. & JACKSON, A. 2016 Magnetic reversals from planetary dynamo waves. *Nature* **539** (7630), 551.
SHISHKINA, O. 2021 Rayleigh-Bénard convection: the container shape matters. *Phys. Rev. Fluids* **6**, 090502.
SHISHKINA, O., HORN, S., WAGNER, S. & CHING, E.S.C. 2015 Thermal boundary layer equation for turbulent Rayleigh–Bénard convection. *Phys. Rev. Lett.* **114**, 114302.
SHISHKINA, O., STEVENS, R.J.A.M., GROSSMANN, S. & LOHSE, D. 2010 Boundary layer structure in turbulent thermal convection and its consequences for the required numerical resolution. *New J. Phys.* **12**, 075022.
VAN DER VEEN, R.C.A., HUISMAN, S.G., DUNG, ON-YU, TANG, H.L., SUN, C. & LOHSE, D. 2016 Exploring the phase space of multiple states in highly turbulent Taylor–Couette flow. *Phys. Rev. Fluids* **1** (2), 024401.
WAGNER, S. & SHISHKINA, O. 2015 Heat flux enhancement by regular surface roughness in turbulent thermal convection. *J. Fluid Mech.* **763**, 109–135.
WALEFFE, F. 1990 On the three-dimensional instability of strained vortices. *Phys. Fluids* **2** (1), 76–80.
WANG, Q., VERZICCO, R., LOHSE, D. & SHISHKINA, O. 2020 Multiple states in turbulent large-aspect ratio thermal convection: What determines the number of convection rolls? *Phys. Rev. Lett.* **125**, 074501.
WANG, Q., WAN, Z.-H., YAN, R. & SUN, D.-J. 2018 Multiple states and heat transfer in two-dimensional tilted convection with large aspect ratios. *Phys. Rev. Fluids* **3** (11), 113503.
WEEKS, E.R., TIAN, Y., URBACH, J.S., IDE, K., SWINNEY, H.L. & GHIL, M. 1997 Transitions between blocked and zonal flows in a rotating annulus with topography. *Science* **278**, 1598–1601.
XI, H.-D. & XIA, K.-Q. 2008 Flow mode transitions in turbulent thermal convection. *Phys. Fluids* **20**, 055104.
XIA, Z., SHI, Y., CAI, Q., WAN, M. & CHEN, S. 2018 Multiple states in turbulent plane Couette flow with spanwise rotation. *J. Fluid Mech.* **837**, 477–490.
XIE, Y.-C., DING, G.-Y. & XIA, K.-Q. 2018 Flow topology transition via global bifurcation in thermally driven turbulence. *Phys. Rev. Lett.* **120**, 214501.
YAO, Z., EMRAN, M.S., TEIMURAZOV, A. & SHISHKINA, O. 2025 Direct numerical simulations of centrifugal convection: from gravitational to centrifugal buoyancy dominance. *Intl J. Heat Mass Transfer* **236**, 126314.
ZHANG, X., ECKE, R.E. & SHISHKINA, O. 2021 Boundary zonal flows in rapidly rotating turbulent thermal convection. *J. Fluid Mech.* **915**, A62.



https://doi.org/10.1017/jfm.2026.11293 Published online by Cambridge University Press

ZHANG, X., VAN GILS, D.P.M., HORN, S., WEDI, M., ZWIRNER, L., AHLERS, G., ECKE, R.E., WEISS, S., BODENSCHATZ, E. & SHISHKINA, O. 2020 Boundary zonal flow in rotating turbulent Rayleigh–Bénard convection. *Phys. Rev. Lett.* **124**, 084505.

ZHANG, X., REITER, P., SHISHKINA, O. & ECKE, R.E. 2024 Wall modes and the transition to bulk convection in rotating Rayleigh–Bénard convection. *Phys. Rev. Fluids* **9**, 053501.

ZIMMERMAN, D.S., TRIANA, A.A. & LATHROP, D.P. 2011 Bi-stability in turbulent, rotating spherical Couette flow. *Phys. Fluids* **23**, 065104.

ZWIRNER, L., TILGNER, A. & SHISHKINA, O. 2020 Elliptical instability and multiple-roll flow modes of the large-scale circulation in confined turbulent Rayleigh–Bénard convection. *Phys. Rev. Lett.* **125**, 054502.

https://doi.org/10.1017/jfm.2026.11293 Published online by Cambridge University Press